**ORIGINAL PAPER**

# Contact Area and Shear Stress in Repeated Single-Asperity Sliding of Steel on Polymer

Xian-Qiang Pei[1,2] · Leyu Lin[2] · Alois K. Schlarb[2,3,4] · Roland Bennewitz[1]

## Abstract

A model for the contact area of a single asperity sliding in a groove after repeated cycles is presented. Based only on the asperity geometry and on data from friction experiments, the model predicts the area of the asymmetric elliptical contact of the asperity sliding in its own groove. It thus allows to determine the shear stress of the steel–polymer couple in the relevant geometry without need for further microscopy of indenter or groove. The model was validated by experiments with an indenter manufactured from slide bearing steel and polyether-ether ketone (PEEK) as substrate. In experiments of 1000 repeated cycles, the contact area was found to vary with varying load and sliding velocity, while the shear stress was 20.5 MPa at a normal pressure of 50–70 MPa, independent of velocity when friction heating is still negligible. Model and experimental confirmation advance single-asperity friction experiments into an efficient method to extract shear stress and contact area for an understanding of sliding friction in metal-polymer contacts.

## 1 Introduction

In friction and wear processes, the contact between surfaces is composed of numerous asperities because of the roughness of engineering materials [1]. Macroscopic friction and wear of tribological systems are governed by the collective action of these asperity contacts [2]. For polymer materials, asperity scratching is one of the most important wear mechanisms that machine components have to withstand during their servicing life [3].

The research strategy of single asperity scratching is to mimic the asperity contacts between rough counterbodies and polymer material surfaces. In most experiments implemented so far, parameters influencing scratch resistance of polymers have been studied. Scratch velocity was reported to influence the scratch damage mode of thermoplastic olefins (TPO), which was categorized as ductile material for scratch velocities around 1 mm/s, while it showed brittle characteristics at 100 mm/s [4]. For a conical indenter with spherical extremity, the normal load governs the contact geometry to be in the spherical or conical part [5]. Connecting friction to wear, the opening angle of conical indenters affected the ploughing friction coefficient [6], while the tip radius had much influence on the wear rate of polymer materials [7]. Mechanical properties and chemical structure were also identified as important factors governing the scratch deformation of polymer materials. For example, the superior resistance to scratch deformation of polypropylenes was ascribed to their high modulus and high yield strength [8]. It was demonstrated that the chemical structure of polyamides had strong influence on their scratch characteristics, where condensation polyamides showed higher scratch hardness than with addition polyamides [9].

Single-stroke scratching experiments reveal distinct mechanisms of wear, but they cannot predict the friction of single asperities in situations which are typical for tribological metal-polymer applications such as slide bearings. In these situations, asperities slide in grooves which are formed by their own repeated interaction with the polymer surface

✉ Xian-Qiang Pei
    xianqiang.pei@mv.uni-kl.de

[1] INM-Leibniz Institute for New Materials,
    66123 Saarbrücken, Germany

[2] Chair of Composite Engineering (CCe), Technische
    Universität Kaiserslautern, 67663 Kaiserslautern, Germany

[3] Research Center OPTIMAS, Technische Universität
    Kaiserslautern, 67663 Kaiserslautern, Germany

[4] Qingdao University of Science and Technology,
    Qingdao 266042, People's Republic of China

[10]. Furthermore, tribofilms of a third material start to form after many cycles at and around asperities and grooves [11]. Here, we report on a model and experiments for friction in often repeated single-asperity sliding. When studying friction mechanisms, the real area of contact is a key parameter [12]. For static non-adhesive contact of a sphere with a flat surface, Hertzian contact mechanics offer well-established methods to calculate the contact size and pressure. When a spherical or conical indenter is sliding against engineering polymers, the contact area is also treated conservatively as a circle in the ASTM international standard for scratch testing, the diameter of which is taken to be the same as the scratch width [13]. For transparent polymers, Gauthier et al. [14, 15] used optical microscopy to monitor the contact area in situ and concluded that the true contact area was the sum of a front half disc and a partial rear half disc. This description highlighted the viscoelastic effects on polymer deformation under tribological loading. The asymmetric shape in leading and trailing side of the indenter is also associated with the different stress state. Compressive stress dominates in the leading side in contrast to tensile stress in the trailing side [16].

The contact geometry changes to sphere-on-groove when a track is formed on the surface upon repeated scratching. The contact of a sphere in a groove is similar to that of a sphere inside a cylinder, which has an elliptical area in the static case [17]. The elliptical shape of the contact area was confirmed experimentally for the continuous sliding of steel balls against polymer coatings in our previous work [18]. Due to the velocity dependence of the contact shape, static contact model can only be used to estimate contact area and contact pressure [19]. In this paper, we present a model for predicting the contact area of a single sliding on a softer surface in steady state after many repeated cycles. We first describe experiments addressing this situation, derive the model, and finally validate the model with the experimental results.

## 2 Experimental

Poly (ether ether ketone) (PEEK, VESTAKEEP® 2000G) plates were used as samples. The sample surfaces were polished in a three step protocol and cleaned before scratch measurements. The plate surface was firstly ground with water sandpaper in the sequence of No. 800, 1200, 2400 and 4000, respectively. Then, the ground surface was further polished with 3, 1 and 0.25 μm diamond pastes. Finally, it was cleaned in acetone in an ultrasonic bath. The roughness of the surface was measured to be 0.027 μm arithmetic average height (Sa).

Scratch tests were conducted on a CSM scratch tester (CSM, Switzerland). To mimic an asperity on a technological steel counterbody, a 100Cr6 steel plate was machined into a cone indenter with spherical tip (Fig. 1). The half apex angle and radius were determined to be 45° and 259 μm, respectively. The long-term friction and wear performance of PEEK were studied by multiple-pass unidirectional scratching in the same track under constant load. Scratch tests lasted for 1000 cycles with normal load spanning from 2.5 to 20 N. The velocity investigated was 100 μm/s and 1000 μm/s, respectively. For each measurement cycle, the scratch force, penetration depth and residual groove depth were recorded. The scratch friction coefficient was calculated as the ratio of scratch force over normal force.

The residual width of scratch grooves was measured using a Keyence VHX-2000D optical microscope (Keyence, Japan). In order to reveal tribological mechanisms, the scratched PEEK surfaces were characterized in a scanning electron microscope (Quanta 400 FEG ESEM, FEI) after sputter-coating with a gold layer.

## 3 Results and Discussion

### 3.1 Friction and Wear of PEEK as Well as Contact Shape in Long-Term Scratching

Figure 2 presents the results of the scratching friction experiments on PEEK. The scratch friction coefficient, penetration depth and the relaxation of the scratch groove are presented for the steady state, which is typically reached after 500 cycles. The friction coefficient increased with increasing normal load, which was also reported for single-asperity scratching of thermoplastic olefins [20] and for macroscopic ball-on-disc experiments on PEEK [21]. The coefficient of friction is 0.31–0.34 at the maximum load of 20 N, a value close to that measured in a cylinder-on-plate configuration [22] and in ball-on-plate tribo-tests [23]. The friction coefficient was found to be about 10% lower when the velocity
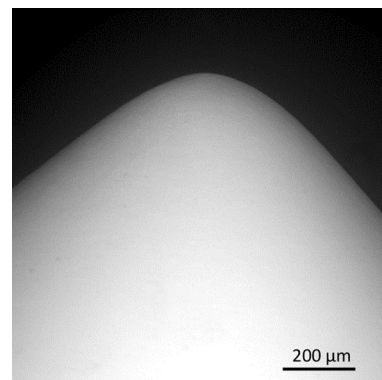


**Fig. 1** SEM micrograph of cross section of the steel indenter (back scattered electron mode, the bright color indicates the indenter)
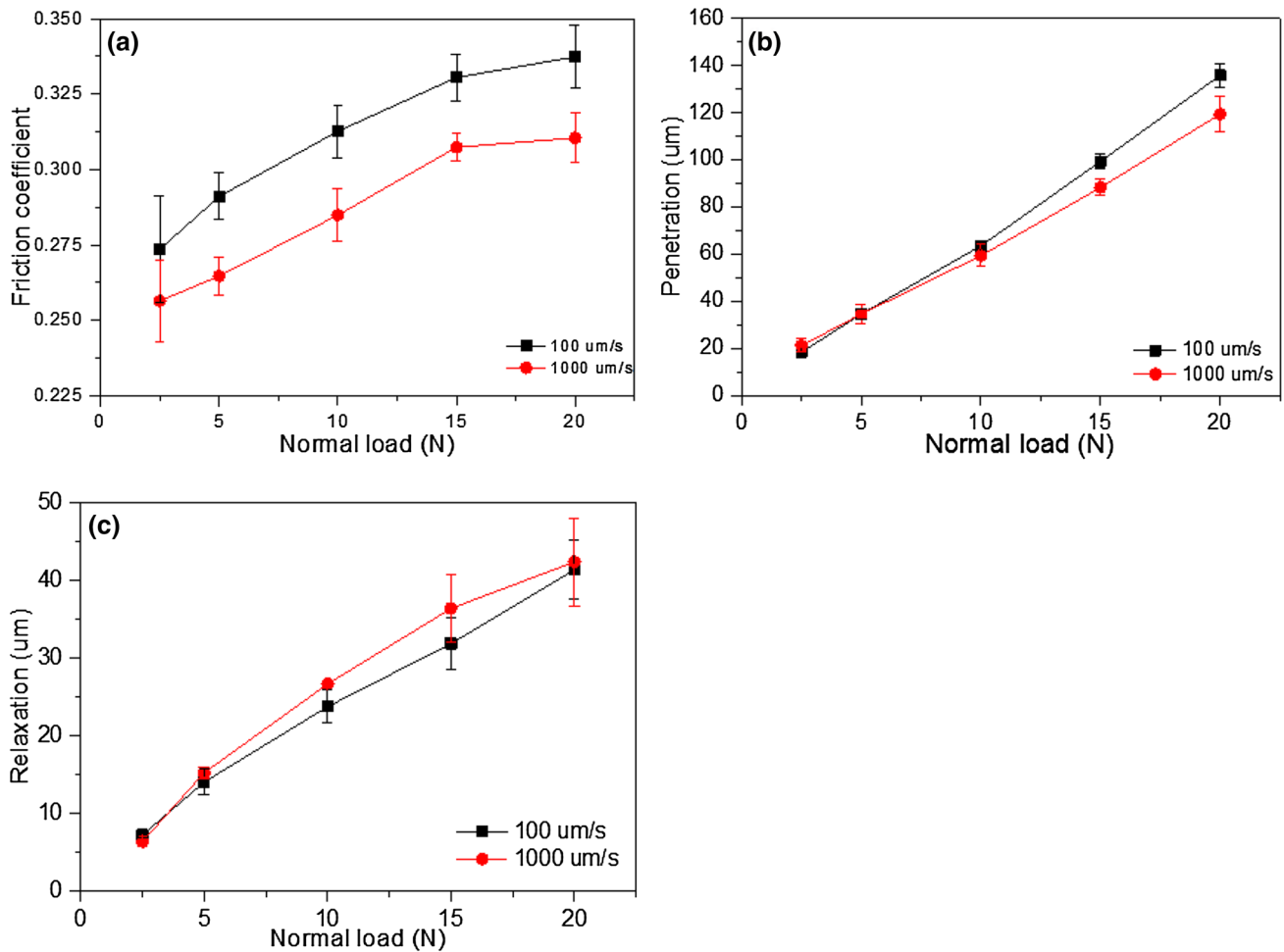
**Fig. 2** Scratching of PEEK by the steel indenter as a function of normal load at different velocities. **a** Steady-state friction coefficient, **b** penetration depth $h_1$ after 1000 cycles, **c** relaxation $h_2$ of the scratch, i.e., difference between penetration depth and residual groove depth

was increased by a factor of ten from 100 to 1000 µm/s (Fig. 2a). The penetration depth was constant in steady state, i.e., ploughing had a negligible contribution to friction in steady state. A lower penetration depth was observed at ten times higher velocity only for loads above 10 N (Fig. 2b). The relaxation depth was independent of velocity within error in the load range investigated (Fig. 2c).

The contact shape was studied by imaging the indenter surface before and after long-term scratching measurements. Figure 3a shows the original surface morphology of the indenter before measurements using the SEM back-scattered electrons detector. Due to the spherical geometry of the indenter top part, the highest intensity of back-scattered electrons is received from the apex area, rendering the apex to the brightest area in the image. By means of a brightness threshold, a circular area was highlighted and the origin of this circle was identified as apex of the indenter (Fig. 3b). Several characteristic grooves were taken as reference to retrieve the apex position of the indenter after scratch tests.

Figure 3d presents one representative surface morphology of the indenter after 1000 cycles of scratching, in which the black contrast reports transferred PEEK materials. The coverage of indenter surface by transferred material varied along the direction of movement. On the leading side, the indenter was covered with material stuck to the indenter surface. Closer inspection reveals a transition from a compact transfer film close to the apex to an area of accumulated clusters farther from the apex. Our main goal in this study is to estimate the real contact area in the scratching process. We identify the transition between compact and agglomerated transfer film with the boundary of the real contact area, indicated by the dashed line in Fig. 3d. On the trailing side, the boundary of the real contact area can be defined from the boundary of an area which is covered in smaller islands of transfer film. Based on symmetry arguments for a sphero-conical asperity sliding in a groove produced by previous scratching cycles, we have chosen an ellipse as contact shape. This choice is justified by the curvature of

**Fig. 3** Image analysis method for studying the contact shape: **a** top-view image of the steel indenter used in the present study (back-scattered electron mode). **b** Brightness thresholding of the image in (a). The indenter apex is identified as the center of the circle. **c** Surface morphology features allow to locate the apex position on the indenter. These features are fine scratches formed during the production of the indenter surface, which are indicated with lines following the orientation of these scratches. **d** Determination of the contact shape (dashed line) with reference to the indenter apex defined in Fig. 3c. The green line indicates the distance from the apex to the edge of the contact area on the leading side, the blue line the distance on the trailing side
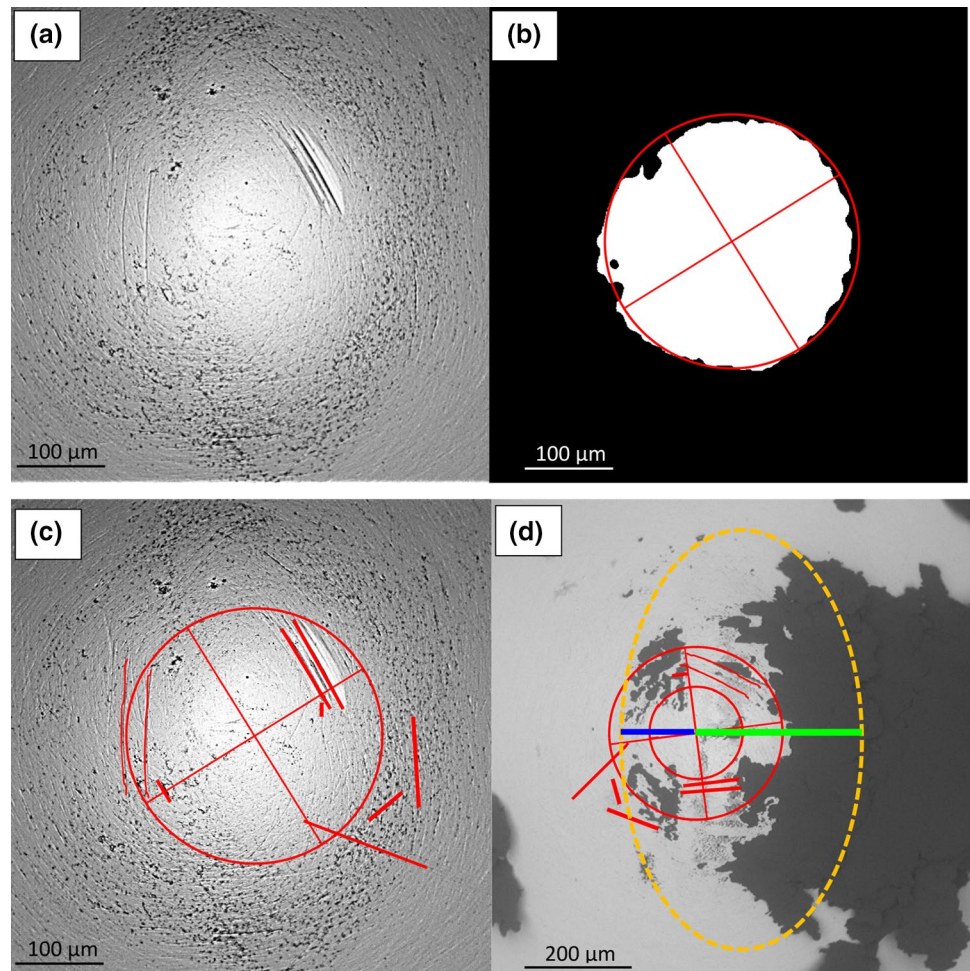


the transition lines and by the successful adaption to many different images of transfer films at the indenters. Note that the center of the ellipse is shifted relative to the apex position (origin of the red circle). The contact area on the leading side of the apex was much larger than that of the trailing side. We conclude that the contact shape in the steady state of multiple scratching of a sphero-conical asperity against a polymer surfaces can be described as an ellipse, whose position is shifted with respect to the apex of the asperity toward the leading side.

The surface morphology of PEEK after long-term scratching is shown in Fig. 4. In general, grooves had well-defined edges along the scratch direction. The residual width of the grooves is summarized in Fig. 5 as a function of normal load for the two tested velocities. For normal loads higher than 5 N the residual groove width was smaller for the higher velocity, consistent with the penetration depth measurement (Fig. 2b). At a low load of 5 N, the worn surfaces exhibited minor scratches running parallel to the groove, indicating the adaption of the grooves' contour to micro-asperities at the indenter

(Fig. 4a, b). The onset of fracture at the worn surfaces was observed for normal loads of 10 N and higher (Fig. 4d). The characteristic features of fracture were also observed on the surface of a PEEK sample subjected to tensile testing (Fig. 4e). This form of surface fracture has previously been ascribed to micro-ductile tearing under tensile stress [24]. The appearance of the fracture features on worn surfaces indicates that the long-term scratch process of PEEK involves mechanisms with tensile failure characteristic.

It has been widely recognized that the velocity dependence of tribological performance of polymers is associated with temperature increase [25]. In the present study with its low sliding velocities, the increase in interfacial temperature can be ignored because it was too small to change the materials properties. It is rather the contact stress which plays the key role in the friction and wear response of PEEK in the current study. Therefore, it is of utmost importance to determine the contact area during scratching. In the following, the calculation of the projected contact area in both normal and lateral direction will be discussed.

**Fig. 4** **a**–**d** Morphology of PEEK surfaces after 1000 cycles of scratching under different load conditions: **a** 5 N, 100 μm/s, **b** 5 N, 1000 μm/s, **c** 10 N, 100 μm/s, **d** 10 N, 1000 μm/s, **e** Morphology of a PEEK surface after tensile testing (50 mm/min)
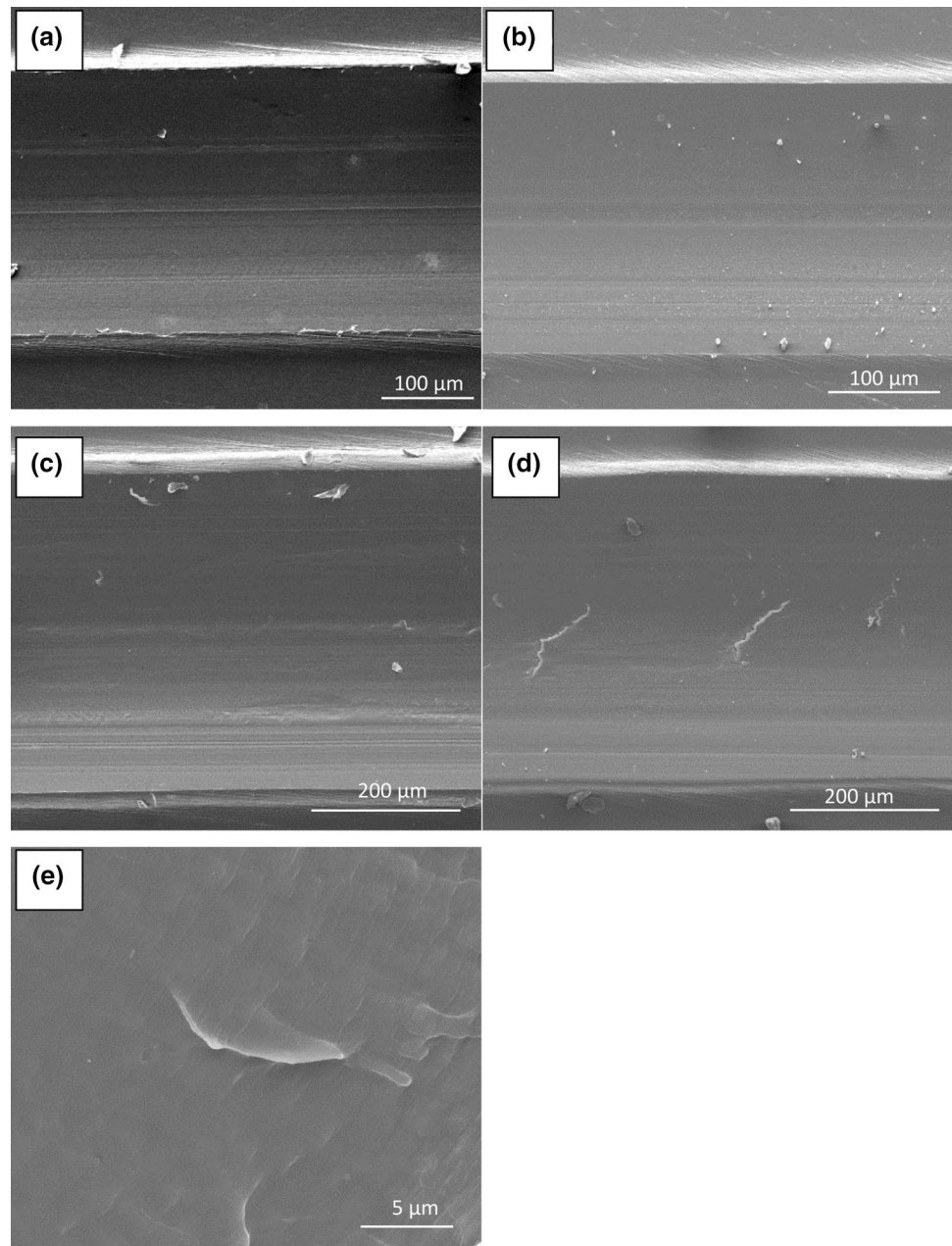
## 3.2 Calculation of Normal Projected Area ($A_n$) and Laterally Projected Area ($A_l$)

We will now establish a method of calculating the elliptical contact area for the sphero-conical indenter sliding in preexisting groove. The parameters of the calculation are the geometrical parameters of indenter and outputs from the tribological tests. Thus, the method will allow to estimate the contact area without additional imaging of the indenter. The symbols and their meanings are listed below:

$\alpha = 45°$ half apex angle of the conical indenter

$R = 259$ μm radius of the spherical indenter

$\beta$ angle comprising tangential and normal force, i.e., $\tan \beta = \frac{F_t}{F_n} = \mu$, in our study $\beta$ was between 14° and 18°

$h_1$ penetration depth of the indenter during the scratching experiment with respect to the surrounding sample surface (Fig. 2b)

$h_2$ relaxation depth, i.e., difference between penetration depth $h_1$ and depth of the relaxed groove after sliding. $h_2$ is determined after each high-load stroke by means of a low-load stroke (Fig. 2c)

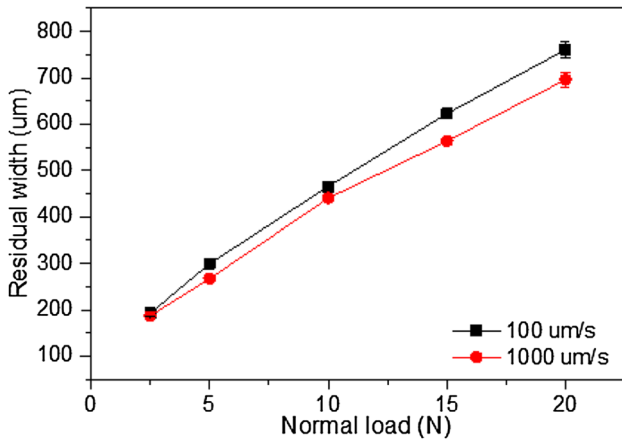$w$ residual width of the grooves left on the surface as determined by optical microscopy (Fig. 5)

**Fig. 5** Residual width of scratch groove as a function of normal load at different velocities

groove follows the projected shape of the indenter, but with material pushed ahead in front the leading side of the indenter. The half major axis a of the contact ellipse is determined as half the measured residual width of the groove and calculated assuming the same relative relaxation as that in depth direction:

$$a = \frac{W}{2} \times \left(1 + \frac{h_2}{h_1}\right) \tag{1}$$

The minor axis of the contact ellipse is composed of two parts, i.e., a rear part ($b_r$) on the trailing side and a front part ($b_f$) on the leading side. The rear part is calculated from the geometry of the indenter:

$$\text{For conical indenter}: \ b_r = h_2 \times \tan \alpha \tag{2}$$

$$\text{For spherical indenter}: \ b_r = \sqrt{R^2 - (R - h_2)^2} \tag{3}$$

The consistency between calculated rear parts by using Eqs. (2) or (3) and measured ones from the SEM images of the indenter after long-term tests can be confirmed for the representative contact shown in Fig. 3d, which was tested under 15 N at 1000 μm/s. The calculated rear contact

*a* half major axis of contact ellipse

b half minor axis of contact ellipse.

Figure 6 schematically illustrates the contact area for an ideal conical and spherical indenter scratching in a preexisting groove. During the measurement, the shape of the

**Fig. 6** Schematic illustration of the contact area model of conical (upper row) and spherical (middle row) indenter moving from left to right: **a** and **c** orthogonal view, **b** and **d** side view and **e** top view of the contact area. Areas are labeled as $A_1$ and $A_n$ corresponding to lateral and normal projected area in side view and top view
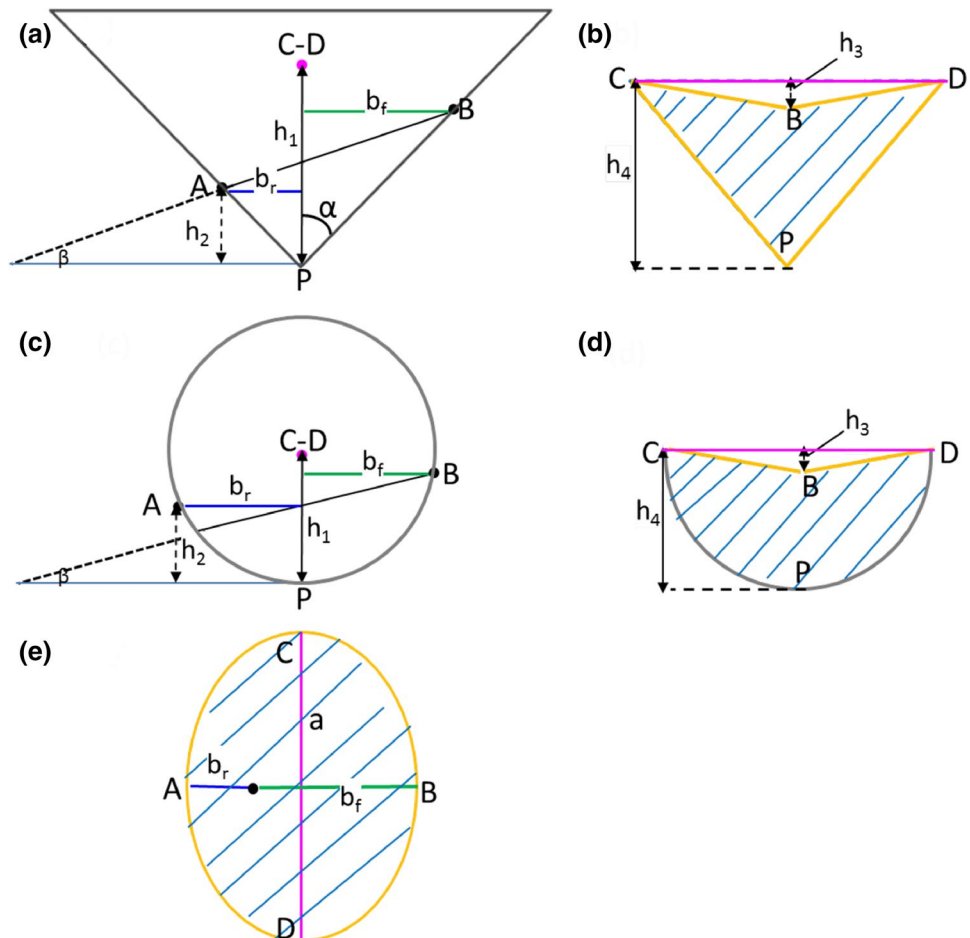
radius is 128 µm, which is close to the measured value of 124 µm.

There is no straightforward prediction for the front minor axis $b_f$ of the contact ellipse. In the following, we suggest an approximation derived from the angle $\beta$, which is defined by points A and B. Point A is the position of contact between indenter and material on the rear side, point B the position of contact between indenter and material on the front side. The angle $\beta$ thus indicates the tilt of an effective shear plane with respect to the sample surface. Let us consider two extreme cases. For fully plastic deformation without relaxation, point A will move to the apex point P and $b_r = 0$. In this case, the angle $\beta$ is the attack angle $\beta = 90 - \alpha$ for perfect ploughing, which according to Bowden and Tabor is related to the ploughing friction coefficient by $\mu_p = 2/\pi \times \tan(90 - \alpha)$ [26]. In the case of full elastic relaxation, points A and B are on the same height, i.e., $b_r = b_f$, $\beta = 0$, and also $\mu = 0$ as there is no dissipation. By interpolation of the two cases, we suggest to approximate

$$\mu = \tan \beta = \frac{F_t}{F_n} \tag{4}$$

This prediction of the angle between surface and effective shear plane has recently been confirmed in in-situ experiments on transparent hydrogels by McGhee et al. [27].

With knowledge of the angle $\beta$ in Fig. 6, the front part of the minor axis can be calculated as follows:

For a conical indenter: $b_f = \dfrac{(b_r \times \tan \beta + h_2) \times \sin \alpha \times \cos \beta}{\sin (90 - \alpha - \beta)}$ (5)

For a spherical indenter: $b_f$
$$= R \times \sin \left[ \beta + a \cos \frac{(R - (b_r \times \tan \beta + h_2) \times \cos \beta)}{R} \right] \tag{6}$$

In the case of a conical indenter with spherical cap, the front part can be determined by combing Eqs. (5) and (6):

$$b_f = \frac{(b_r \times \tan \beta + h_2 + l_0) \times \sin \alpha \times \cos \beta}{\sin (90 - \alpha - \beta)} \tag{7}$$

In Eq. (7), $l_0$ is the height difference between the end of a spherical cap and the end of the full cone

$$l_0 = R \times \left( \frac{1}{\sin \alpha} - 1 \right) \tag{8}$$

The half minor axis of contact ellipse is then : $b = \dfrac{b_r + b_f}{2}$ (9)

Finally, the normal projected area ($A_n$) can be calculated using the following equation:

$$A_n = \pi \times a \times b \tag{10}$$

Thanks to the formation of transfer films on the indenter surface, the front and rear contact length can be determined by the image analysis introduced above. Table 1 compares calculated and measured contact lengths. Their similarity validates our contact model.

The laterally projected contact area is depicted in Fig. 6b, d for conical and spherical indenters. Its area can be calculated as the difference between a triangle (conical indenter) and a circular segment (spherical indenter) with a height of $h_4$ and a small triangle with a height of $h_3$.

For conical indenter:

$$h_4 = \frac{a}{\tan \alpha} \tag{11}$$

$$h_3 = h_4 - \frac{b_f}{\tan \alpha} = \frac{a - b_f}{\tan \alpha} \tag{12}$$

$$A_1 = a \times (h_4 - h_3) = \frac{a \times b_f}{\tan \alpha} \tag{13}$$

For spherical indenter:

$$h_4 = R - \sqrt{R^2 - a^2} \tag{14}$$

$$h_3 = h_4 - \left[ (b_r + b_f) \times \tan \beta + h_2 \right] \tag{15}$$

$$A_1 = a \sin \frac{a}{R} \times R^2 - a \times R \times \cos \left( a \sin \frac{a}{R} \right) - a \times h_3 \tag{16}$$

In the current study, the indenter was sphero-conical and can be considered as a combination of ideal conical and spherical indenters. The contact area in this case is shown in Fig. 7.

For simplicity, symbols with the same denotation as in Fig. 6 are not repeated. Two new symbols have to be introduced due to the combination of sphere and cone for the indenter used.

Height at sphere-to-cone transition: $h_t = R \times (1 - \sin \alpha)$ (17)

**Table 1** Comparison of the contact lengths $b_f$ and $b_r$ from calculation and image analysis

| | $b_f$ (µm) | | $b_r$ (µm) | |
|---|---|---|---|---|
| | Calculated | Measured | Calculated | Measured |
| 100 µm/s, 15 N | 290 | 285 | 130 | 123 |
| 100 µm/s, 20 N | 305 | 310 | 134 | 137 |
| 1000 µm/s, 15 N | 276 | 283 | 137 | 127 |
| 1000 µm/s, 20 N | 298 | 290 | 148 | 156 |

**Fig. 7** Contact area of a sphero-conical indenter scratching in a preexisting groove on polymer surface: **a** orthogonal view and **b** side view with respect to the scratch direction from left to right
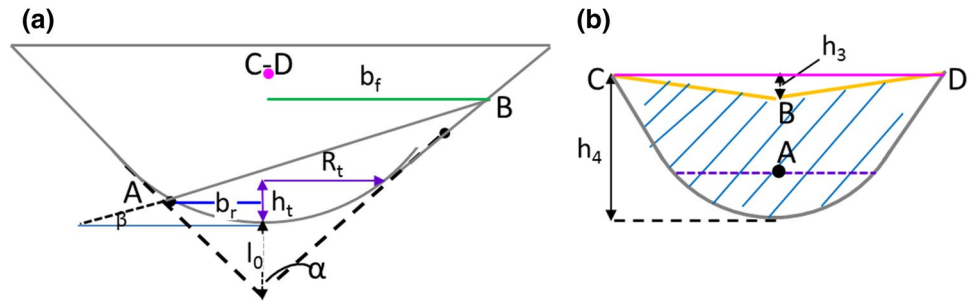


Radius at sphere-to-cone transition : $R_t = R \times \cos \alpha$

$$(18)$$

The lateral area is the sum of areas below and above the transition line from sphere to cone (dotted purple line in Fig. 7b).

Lateral area below sphere-to-cone transition:

$$A_{l1} = a \sin \frac{R_t}{R} \times R^2 - R_t \times R \times \cos \left( a \sin \frac{R_t}{R} \right) \qquad (19)$$

$$h_3 = \frac{a - b_f}{\tan \alpha} \qquad (20)$$

Lateral area above sphere-to-cone transition:

$$A_{l2} = (a + R_t) \times \left( \frac{a}{\tan \alpha} - h_t - l_0 \right) - a \otimes h_3 \qquad (21)$$

The lateral contact area shown in Fig. 7b is a representative illustration in which the front contact boundary lies above the sphere-to-cone transition. When the front contact boundary lies below this transition, the lateral contact area should be calculated by Eq. (16) for spherical indenters.

## 3.3 Application of Our Contact Area Model in Studying the Friction Mechanisms of PEEK

Following the method established in the preceding part, the normal contact area and the ratio between major and minor axes of the contact ellipse were calculated for our experiments (see Fig. 8). The normal contact area increased linearly with increasing normal load, which is in contrast to a sub-linear relation expected for an elastic Hertzian contact with a flat substrate. The normal contact area was slightly smaller for the ten times higher velocity, and this decrease in contact area became more significant at higher load. A similar dependence was found for the friction coefficient (Fig. 2a), indicating correlation between the real contact area and friction. The lower friction coefficient for the higher velocity can be related to the smaller contact area. The ellipticity of the contact area changed from almost circular contacts at low loads to an ellipticity of more than 2 at high loads. The difference in ellipticity for the two velocities was small and insignificant.

The knowledge of contact area allows us to calculate the real contact pressure under the indenter during the long-term scratching. Figure 9a presents the normal contact pressure as
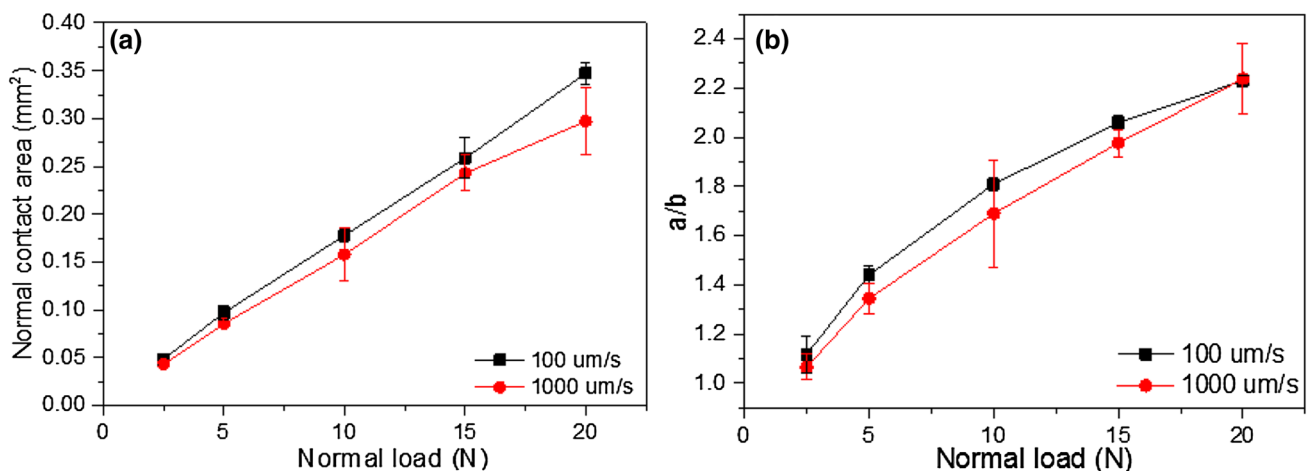


**Fig. 8** **a** Calculated normal contact area and **b** ratio between major and minor axes of the contact ellipse as a function of normal load at different velocities

function of the normal load. At a velocity of 100 μm/s, the contact pressure was between 52 MPa at a load of 2.5 N and 58 MPa at a load of 20 N. At a velocity of 1000 μm/s, the contact pressure was about 10% higher, ranging from 58 MPa to 67 MPa. These pressure values are of the same magnitude as the scratch hardness of PEEK reported by Stuart et al. [28]. The increase in contact pressure can be explained by a change in the contact geometry. For small load and shallow grooves, the circular normal contact area was almost identical to the full contact between indenter and substrate. For high load and deeper grooves, the elliptical normal contact also involved contact between the indenter and the slopes of the groove which contributed to the load bearing.

The lateral force is plotted versus the normal contact area in Fig. 9b. In contrast to all results presented so far, data points for the two velocities lie on one curve in this presentation, indicating that the characteristic of the curve reveals a velocity-independent tribological property. According to Bowden and Tabor [29], a linear relation between lateral force and contact area indicates a shearing dominated friction process, and the slope of this plot can be considered as the interfacial shear strength, which is found to be 20.5 MPa for our steel indenter sliding against PEEK. This value compares well to the 15 MPa reported by Briscoe et al. [30] for sliding of PEEK on glass at a pressure of about 28.5 MPa. The difference of 5.5 MPa in shear stress can be explained by the difference of about 30 MPa in the normal pressure and the pressure factor of PEEK, reported to be in the range of $0.2 \pm 0.05$ by Briscoe [30].

This analysis of Fig. 9b in terms of shear stress is based on the assumption that all lateral force originates from shear mechanisms. However, we derived our result from a geometry with a tilted effective shear plane, i.e., with a deformation moving with the sliding asperity. Therefore, we also must consider viscous contributions to friction. The lateral contact area, i.e., the projection of the contact area in the direction of sliding, is plotted in Fig. 10 as function of the normal load for the two velocities. The lateral contact area increased linearly with increasing normal load with only little influence of the velocity. Following a description of viscoelastic friction in asperity sliding given by Popov [31], the viscoelastic friction coefficient can be estimated as

$$\mu_{visc} = \xi \nabla z \frac{G''(v/r)}{\left| \hat{G}(v/r) \right|} \tag{22}$$

where $\xi$ is a dimensionless parameter of order 1, $\nabla_z$ is the average gradient of the surface profile, $G''$ is the dissipative part of the shear modulus, $\left| \hat{G} \right|$ is the absolute magnitude of the shear modulus, and $(v/r)$ is the effective frequency of excitation, given as the ratio of the sliding velocity $v$ and the characteristic lateral extension $r$ of one asperity.
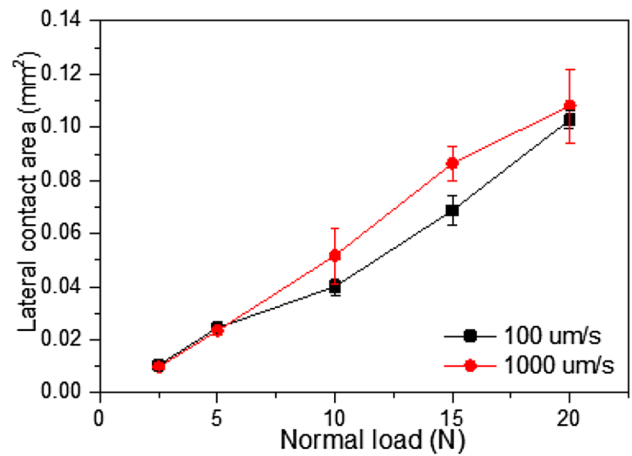


**Fig. 10** Lateral contact area as function of normal load at different velocities
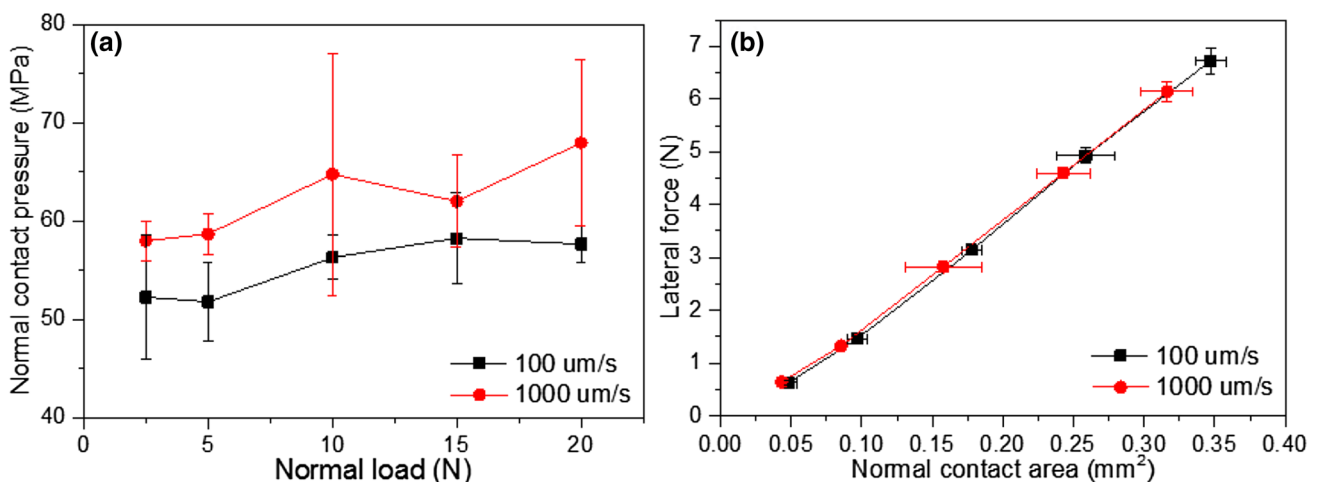


**Fig. 9 a** Normal contact pressure as function of normal load. **b** Lateral force as function of normal contact area at different velocities

We will estimate $\mu_{visc}$ for two limiting cases, assuming first the steel indenter as a single asperity and assuming second the roughness of the slider as source of viscous friction. Looking at the steel indenter as single asperity, the average surface gradient is the tilt of the shear plane as in Eq. 4 with $\nabla_z = \tan\beta = \mu$. With $(v/r) \approx 1\,\text{Hz}$, $G'' = 56\,\text{MPa}$ and $\left|\hat{G}\right| = 4110\,\text{MPa}$. We find that $\mu_{visc} \approx 0.1\mu$, so that viscous contributions may have led to an overestimation of the shear stress of the order of 10%.

The average surface gradient given by the indenter's roughness can be estimated as $\nabla_z = 2\langle\sigma\rangle/E^*$ (Popov), where the average contact pressure $\langle\sigma\rangle = 60\,\text{MPa}$ (see Fig. 9) and $E^* = 4320\,\text{MPa}$ for PEEK. Since $G''/\left|\hat{G}\right| < 1$, we can safely neglect the roughness contribution to $\mu_{visc}$. All values for the shear modulus were determined by dynamic mechanical analysis.

To understand its role in friction, the lateral contact area should be understood simply as the projection of the tilted effective shear plane (Eq. 4) into the direction of sliding motion. Accordingly, the increase in lateral contact area with increasing normal load (Fig. 10) is proportional to the increase of normal contact area. This relation can also be observed in the morphology of the transfer layer (Fig. 11) on the leading side. For a normal load of 5 N, the leading-side of the contact area was covered with sparse patches of transfer film (Fig. 11a, c), corresponding to a very small lateral contact area (Fig. 10). For a normal force of 10 N, the leading side of the contact was densely covered with a compact transfer layer (Fig. 11b, d). We believe that localized plastic flow process took place along the indenter surface [32] and contributed to the formation of transfer layers. Overall, friction mostly arises from the shear and plastic flow between the indenter and the slightly tilted effective shear plane. Most of the contact area appears in normal projection and a small part of it in lateral projection. The lateral contact area does not indicate an extra mechanism in frictional dissipation but the deflection of the effective shear plane.

# 4 Conclusions

A model was developed to calculate the contact area between a hard sphero-conical indenter and a groove in a softer surface upon repeated cycles of sliding. The input parameters

**Fig. 11** Morphology of transferred PEEK on indenter surface after 1000 cycles of scratching under different load conditions: **a** 5 N, 100 μm/s, **b** 10 N, 100 μm/s, **c** 5 N, 1000 μm/s, **d** 10 N, 1000 μm/s
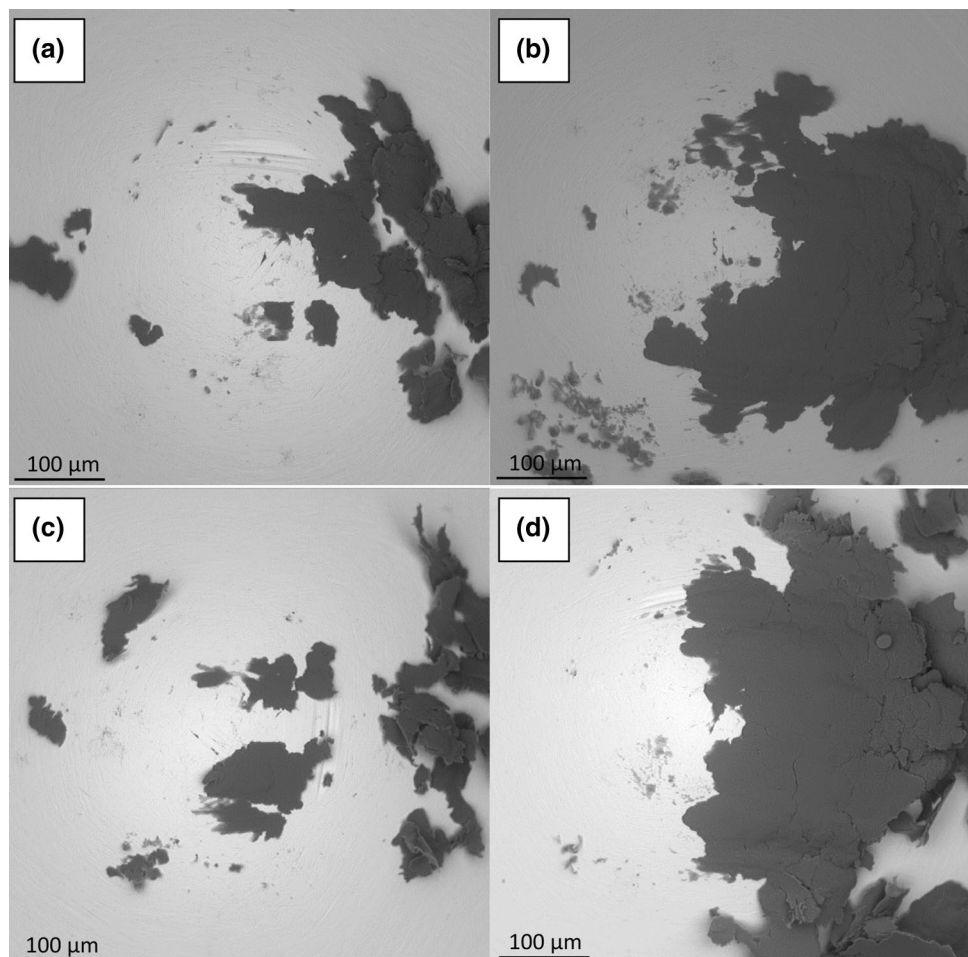
of the model are the geometry of the indenter (radius of apex, opening angle of cone) and quantities measured in the tribological experiment (friction coefficient, actual and residual penetration depth). The model allows to determine the area of contact without additional imaging of indenter or surface. It takes into account the elliptical shape of the contact between indenter and groove and its asymmetry with respect to the indenter apex upon sliding. The key assumption of the model is that the geometric tilt of the effective shear plane with respect to the surface is proportional to the friction coefficient.

The model was validated in experiments with a single-asperity indenter manufactured from standard slide bearing steel and PEEK as substrate, where a large number of cycle repetitions mimicked the situation in slide bearings. Optical and electron microscopy confirms the correct prediction of the contact area and its displacement with respect to the tip apex. The model allows to determine the steel-PEEK shear stress for the single-asperity experiment, and numbers are in agreement with previous reports. Experiments at low velocities varying by a factor of ten result in significantly different friction and penetration values. However, applying our contact area model we find that the shear stress is independent of velocity, as expected at low velocities where friction does not lead to temperature increase.

Single-asperity friction experiments are a key strategy for understanding mechanisms in friction and wear of realistically rough surfaces. The new model correctly predicts the contact area for the complex but realistic situation of an asperity sliding repeatedly in its own groove of a softer surface. It allows to determine the shear stress for the material couple after repeated cycles in the relevant geometry. Model and experimental confirmation advance single-asperity friction experiments into an efficient method to extract shear stress and contact area for an understanding of sliding friction in metal-polymer contacts.

# References

1. Bowden, F.P., Moore, A.J.W., Tabor, D.: The ploughing and adhesion of sliding metals. J. Appl. Phys. **14**(2), 80–91 (1943). https://doi.org/10.1063/1.1714954
2. Gane, N., Bowden, F.P.: Microdeformation of solids. J. Appl. Phys. **39**(3), 1432–1435 (1968). https://doi.org/10.1063/1.1656376
3. Iqbal, T., Yasin, S., Luckham, P.F., Ramzan, N., Mohsin, M.: Scratch deformations of poly (ether ether ketone) composites. Fibers Polym. **15**(5), 1042–1050 (2014). https://doi.org/10.1007/s12221-014-1042-x
4. Jiang, H., Browning, R., Sue, H.-J.: Understanding of scratch-induced damage mechanisms in polymers. Polymer. **50**(16), 4056–4065 (2009). https://doi.org/10.1016/j.polymer.2009.06.061
5. Krupička, A., Johansson, M., Hult, A.: Use and interpretation of scratch tests on ductile polymer coatings. Prog. Org. Coat. **46**(1), 32–48 (2003). https://doi.org/10.1016/S0300-9440(02)00184-4
6. Briscoe, B.J., Evans, P.D., Lancaster, J.K.: Single point deformation and abrasion of γ-irradiated poly(tetrafluoroethylene). J. Phys. D **20**(3), 346 (1987)
7. Woldman, M., Van Der Heide, E., Tinga, T., Masen, M.A.: The influence of abrasive body dimensions on single asperity wear. Wear. **301**(1–2), 76–81 (2013). https://doi.org/10.1016/j.wear.2012.12.009
8. Hadal, R.S., Misra, R.D.K.: Scratch deformation behavior of thermoplastic materials with significant differences in ductility. Mater. Sci. Eng. A **398**(1–2), 252–261 (2005). https://doi.org/10.1016/j.msea.2005.03.028
9. Rajesh, J.J., Bijwe, J.: Investigations on scratch behaviour of various polyamides. Wear. **259**(1–6), 661–668 (2005). https://doi.org/10.1016/j.wear.2004.12.018
10. Bermudez, M.D., Brostow, W., Carrion-Vilches, F.J., Cervantes, J.J., Pietkiewicz, D.: Wear of thermoplastics determined by multiple scratching. e-Polymers 001 (2005)
11. Pei, X.-Q., Lin, L.-Y., Schlarb, A.K., Bennewitz, R.: Novel experiments reveal scratching and transfer film mechanisms in the sliding of the PEEK/steel tribosystem. Tribol. Lett. **63**(3), 1–9 (2016). https://doi.org/10.1007/s11249-016-0732-5
12. Bowden, F.P., Tabor, D.: The area of contact between stationary and between moving surfaces. Proc. R. Soc. Lond. **169**(938), 391–413 (1939)
13. D7027-13, A: Standard Test Method for Evaluation of Scratch Resistance of Polymeric Coatings and Plastics Using an Instrumented Scratch Machine. ASTM International, West Conshohocken (2013) http://www.astm.org
14. Gauthier, C., Lafaye, S., Schirrer, R.: Elastic recovery of a scratch in a polymeric surface: experiments and analysis. Tribol. Int. **34**(7), 469–479 (2001). https://doi.org/10.1016/S0301-679X(01)00043-3
15. Lafaye, S., Gauthier, C., Schirrer, R.: Analysis of the apparent friction of polymeric surfaces. J. Mater. Sci. **41**(19), 6441–6452 (2006). https://doi.org/10.1007/s10853-006-0710-7
16. Malzbender, J., den Toonder, J.M.J., Balkenende, A.R., de With, G.: Measuring mechanical properties of coatings: a methodology applied to nano-particle-filled sol–gel coatings on glass. Mater. Sci. Eng. **36**(2), 47–103 (2002). https://doi.org/10.1016/S0927-796X(01)00040-7
17. Puttock, M.J., Thwaite, E.G.: Elastic compression of spheres and cylinders at point and line contact. National Standards Laboratory Technical Paper No. 25 Commonwealth Scientific and Industrial Research Organization, Australia (1969)
18. Pei, X.-Q., Bennewitz, R., Kasper, C., Tlatlik, H., Bentz, D., Becker-Willinger, C.: Tribological synergy of filler components in multi-functional polyimide coatings. Adv. Eng. Mater. **19**(1), 1600363 (2017)
19. Villat, C., Ponthiaux, P., Pradelle-Plasse, N., Grosgogeat, B., Colon, P.: Initial sliding wear kinetics of two types of glass ionomer cement: a tribological study. Biomed. Res. Int. (2014). https://doi.org/10.1155/2014/790572
20. Jiang, H., Browning, R., Fincher, J., Gasbarro, A., Jones, S., Sue, H.-J.: Influence of surface roughness and contact load on friction coefficient and scratch behavior of thermoplastic olefins. Appl. Surf. Sci. **254**(15), 4494–4499 (2008). https://doi.org/10.1016/j.apsusc.2008.01.067

21. Zhang, G., Liao, H., Li, H., Mateus, C., Bordes, J.M., Coddet, C.: On dry sliding friction and wear behaviour of PEEK and PEEK/SiC-composite coatings. Wear. **260**(6), 594–600 (2006). https://doi.org/10.1016/j.wear.2005.03.017

22. Rzatki, F.D., Barboza, D.V.D., Schroeder, R.M., Barra, G.M.d.O., Binder, C., Klein, A.N., de Mello, J.D.B.: Effect of surface finishing, temperature and chemical ageing on the tribological behaviour of a polyether ether ketone composite/52100 pair. Wear. **332–333**, 844–854 (2015). https://doi.org/10.1016/j.wear.2014.12.035

23. Schroeder, R., Torres, F.W., Binder, C., Klein, A.N., de Mello, J.D.B.: Failure mode in sliding wear of PEEK based composites. Wear. **301**(1–2), 717–726 (2013). https://doi.org/10.1016/j.wear.2012.11.055

24. Chen, F., Ou, H., Gatea, S., Long, H.: Hot tensile fracture characteristics and constitutive modelling of polyether-ether-ketone (PEEK). Polym. Testing. **63**, 168–179 (2017). https://doi.org/10.1016/j.polymertesting.2017.07.032

25. Laux, K.A., Jean-Fulcrand, A., Sue, H.J., Bremner, T., Wong, J.S.S.: The influence of surface properties on sliding contact temperature and friction for polyetheretherketone (PEEK). Polymer. **103**, 397–404 (2016). https://doi.org/10.1016/j.polymer.2016.09.064

26. Bowden, F.P., Tabor, D.: Friction, lubrication and wear: a survey of work during the last decade British. J. Appl. Phys. **17**(12), 1521–1544 (1966)

27. McGhee, E.O., Pitenis, A.A., Urueña, J.M., Schulze, K.D., McGhee, A.J., O'Bryan, C.S., Bhattacharjee, T., Angelini, T.E., Sawyer, W.G.: In situ measurements of contact dynamics in speed-dependent hydrogel friction. Biotribology. **13**, 23–29 (2018). https://doi.org/10.1016/j.biotri.2017.12.002

28. Stuart, B.H., Briscoe, B.J.: The effect of crystallinity on the scratch hardness of poly(ether ether ketone). Polym. Bull. **36**(6), 767–771 (1996). https://doi.org/10.1007/bf00338642

29. Bowden, F.P., Tabor, D.: The Friction and Lubrication of Solids, (Vol. 2). Clarendon Press, Oxford (1964)

30. Briscoe, B.J., Stuart, B.H., Sebastian, S., Tweedale, P.J.: The failure of poly (ether ether ketone) in high speed contacts. Wear **162–164**, 407–417 (1993). https://doi.org/10.1016/0043-1648(93)90524-P

31. Popov, V.: Contact Mechanics and Friction: Physical Principles and Applications (Vol. 55), Springer, Amsterdam (2010)

32. Bellemare, S., Dao, M., Suresh, S.: The frictional sliding response of elasto-plastic materials in contact with a conical indenter. Int. J. Solids Struct. **44**(6), 1970–1989 (2007). https://doi.org/10.1016/j.ijsolstr.2006.08.008